Materials Advances

ROYAL SOCIETY OF CHEMISTRY

PAPER

View Article Online
View Journal | View Issue

Cite this: *Mater. Adv.*, 2025, 6, 1423

Design and investigation of a new two-dimensional cobalt metal–organic framework for highly sensitive electrochemical detection of the nitrofurazone drug in food and biological samples†

T. Leelasree[a] and Himanshu Aggarwal *[ab]

Received 21st November 2024,
Accepted 13th January 2025

DOI: 10.1039/d4ma01152j

rsc.li/materials-advances

Antibiotic pollution poses a significant threat to global health and ecosystems. It is highly demanding to detect the trace amounts of antibiotics in food and biological samples. Thus, there is a critical need for rapid and sensitive sensors with real-time monitoring capabilities to address this challenge. In this regard, porous materials such as metal–organic frameworks (MOFs) with unique and tailorable properties can serve as highly sensitive sensors for the detection of targeted analytes. Here, a new two-dimensional cobalt MOF (2D-Co MOF) has been designed and studied for the detection of nitrofurazone (NFZ), a nitrofuran class antibiotic. The 2D-Co MOF sensor demonstrates exceptional sensitivity in detecting NFZ, achieving a remarkably low detection limit of 0.04 μM. The MOF system also displayed excellent selectivity towards NFZ in the presence of potential interferants, thus acting as a potent sensor for the detection of NFZ. Additionally, the sensor exhibits excellent reliability and stability. To further demonstrate the practical applicability, the MOF sensor has been explored for the detection of NFZ drug residues in food and biological samples.

1. Introduction

Globally, the production and utilization of antibiotics have significantly spiked due to the outburst of COVID-19,[1,2] thus leading to more pharmaceutical waste. Lack of consumer education on the disposal of expired medicines and unregulated manufacturing of antibiotics lead to improper disposal of antibiotics to the surroundings. These antibiotics enter the wastewater systems affecting marine life and causing severe antibiotic pollution. Antibiotics also suffer from degradation difficulty, inducing detrimental effects on the environment. Antibiotics are also administered to farm animals to treat diseases and increase productivity, thus leading to the contamination of food products. Antibiotic pollution is highly associated with antibiotic resistance increasing the risk of humans to multiple health issues and diseases.[3,4] In this regard, the nitrofuran class of antibiotics, such as nitrofurazone (NFZ), have been widely used to treat bacterial, microbial and protozoan infections in farm and veterinary animals.[5,6] Nevertheless, the utilization of these substances has been prohibited due to the observed occurrence of tumor development in livestock and the potential carcinogenic effects. Also, the use of NFZ in food-producing farm animals will eventually leave traces of the drug in the meat, milk, and other products they produce. Additionally, there have also been reports of cancer, functional impairments, and mutagenic hazards in human consumers as a result of the consumption of these animal products *via* the food chain.[7,8] Highly sensitive, selective, and rapid methods of analysis are typically necessary for studying quantities at such low levels.

To date, several analytical techniques and spectroscopy methods including UV-visible spectroscopy, fluorescence spectroscopy, Raman spectroscopy, and mass spectrometry have been employed for the detection of NFZ.[9–14] However, these techniques demand time-intensive procedures and laborious sample preparations. Additionally, substances should adhere to the strict analytical method protocols to meet the instrument requirements. On the contrary, electrochemical methods are highly preferred for the detection of NFZ due to their high sensitivity, wide signal range, quick detection time, convenient portability, and simple preparation methods.[15–17]

The incessant pursuit in the field of electrochemical sensor manufacturing warrants designing an efficient sensor

[a] *Department of Chemistry, Birla Institute of Technology and Science, Hyderabad Campus, Hyderabad 500078, India.*
E-mail: himanshu.aggarwal@hyderabad.bits-pilani.ac.in
[b] *Materials Center for Sustainable Energy & Environment (McSEE), Birla Institute of Technology and Science, Hyderabad Campus, Hyderabad 500078, India*

† Electronic supplementary information (ESI) available. CCDC 2391733. For ESI and crystallographic data in CIF or other electronic format see DOI: https://doi.org/10.1039/d4ma01152j

with high sensitivity, stability, and selectivity towards low analyte levels in real samples. Electrochemical sensors based on nanomaterials, metal oxides, reduced graphene oxides, carbon nanotubes, and boron-based materials have been extensively studied to detect NFZ.[18–23] Metal–organic frameworks (MOFs), a class of advanced porous materials, have emerged as versatile and effective sensors, owing to their exceptional surface areas and distinct properties. Moreover, due to their structural diversity, high stability, and controlled porosity, MOFs are desirable candidates for diverse applications.[24–29]

Significant research efforts have been made to design MOF materials with preferred structural environments and desired properties for targeted applications. Furthermore, structuring MOFs with customizable pore sizes by carefully selecting inorganic and organic building units enables efficient adsorption and selective recognition of target analytes, which ultimately enhances MOF's affinity and sensitivity towards an analyte even at low concentrations. Herein, we have synthesized a new 2D-Co MOF by a mixed-linker approach under solvothermal conditions and studied it for the detection of NFZ antibiotic.

2. Experimental details

2.1 Materials

Cobalt nitrate hexahydrate $[Co(NO_3)_2{\cdot}6H_2O]$ was purchased from SRL chemicals, 2,6-naphthalene dicarboxylic acid, 1,4,5,8-naphthalene tetracarboxylic dianhydride, 4-aminopyridine, and nitrofurazone was purchased from TCI chemicals. All the solvents were purchased from SRL chemicals and used as such without further purification.

2.2 Synthesis of DPNDI

The ligand *N*,*N*′-di(4-pyridyl)-1,4,5,8-naphthalenetetracarboxydiimide (DPNDI) was synthesized according to the reported procedure with some modifications.[30] 3 mmol of 1,4,5,8-naphthalene tetracarboxylic dianhydride and 6 mmol of 4-aminopyridine were mixed in 25 ml of *N*,*N*-dimethylformamide (DMF) and allowed to reflux for 12 h. A crystalline solid precipitated out on cooling to room temperature. The obtained solid was collected by filtration and was further purified by recrystallization from DMF. The recrystallized product was filtered and dried in a vacuum oven at 80 °C for 8 h to obtain crystalline DPNDI ligand (81% yield). The purity of the obtained product was confirmed by ^{1}H NMR and mass spectroscopy. ^{1}H NMR of DPNDI was recorded in a mixture of DMF and DMSO-d_6 solvent at 298 K. ^{1}H NMR (400 MHz): δ = 8.81 (d, 4H), 8.75 (s, 4 H) and 7.59 (d, 4H) ppm. DMF: δ = 7.95, 2.89 and 2.73 ppm. DMSO-d_6: δ = 2.50 ppm (Fig. S1, ESI†). MS-*m*/*z*: calculated for $C_{24}H_{12}N_4O_4$, exact mass: 420.09, found: 420 (Fig. S2, ESI†).

2.3 Synthesis of 2D-Co MOF

A mixture of $[Co(NO_3)_2{\cdot}6H_2O]$ (0.4 mmol), 2,6-naphthalene dicarboxylic acid (2,6-NDC) (0.2 mmol) and *N*,*N*′-di(4-pyridyl)-1,4,5,8-naphthalenetetracarboxydiimide (DPNDI) (0.2 mmol) in 3 : 1 (v/v) ratio of DMF and methanol was taken in a vial and sonicated for 30 min to obtain a clear solution. The reaction mixture was heated at 80 °C for 5 days. The obtained light brown crystals were washed and analyzed for further characterization.

2.4 Single-crystal X-ray diffraction (SC-XRD) analysis

SC-XRD studies of the crystals were performed on a Rigaku XtaLAB P200 diffractometer with Cu-Kα radiation (λ = 1.54184 Å) at 100 K. The crystallographic data collection and reduction were performed using the CrysAlisPro software program. Olex2 with the ShelXT structure solution program was used to solve the structure and further refined with the help of the ShelXL refinement package using least squares minimization. The crystallographic data is tabulated in Table S1, ESI.†

2.5 Electrochemical measurements

Cyclic voltammetry (CV) measurements were carried out using Origaly's France-OGF 0500 Model electrochemical workstation with OrigaMaster5 software. CVs were recorded using a three-electrode electrochemical set-up, where a MOF-coated glassy carbon electrode (GCE) acts as the working electrode, platinum wire as the counter electrode, and Ag/AgCl as the reference electrode. The electrolyte used for the study was 0.1 M phosphate buffer solution (PBS).

To obtain a MOF-coated GCE, the MOF sample was gently ground and a uniform MOF suspension was prepared in ethanol. 10 μL of the MOF suspension was drop cast onto the polished bare GCE and dried, followed by the addition of 3 μL Nafion as a binder and allowed to dry at room temperature. The MOF-coated GCE was used for the electrochemical measurements.

2.6 Characterization techniques

Powder X-ray diffraction (PXRD) analysis was performed using a Rigaku Ultima-IV diffractometer with Cu-Kα radiation (40 kV, 40 mA). The PXRD patterns were acquired in the 2θ range of 5°–40° with a step size of 1° min^{-1}. Thermogravimetric analysis (TGA) was performed using the Shimadzu DTG-60 instrument. The analysis was carried out under a N_2 atmosphere by maintaining a heating rate of 10 °C min^{-1} in the temperature range of 30 °C to 800 °C. N_2 sorption studies were carried out using a Microtrac Bel – BEL SORP mini II model surface area analyzer. The MOF sample was activated at 200 °C before proceeding to the N_2 adsorption measurements. Field emission scanning electron microscopy (FE-SEM) analysis was performed using the FEI Apreo LoVac instrument. X-ray photoelectron spectroscopy (XPS) studies were performed with the help of a Thermo Scientific K-α instrument [Al K-α source, X-ray source 1486.8 eV]. ^{1}H NMR was recorded on a Bruker AV NEO 400 MHz instrument. Mass spectral data was obtained using an LCMS-8040 (Shimadzu) mass spectrometer.

3. Results and discussion

3.1 Structural details and characterization of the MOF

The MOF crystals were synthesized solvothermally by using a mixed-linker approach by reacting the metal salt

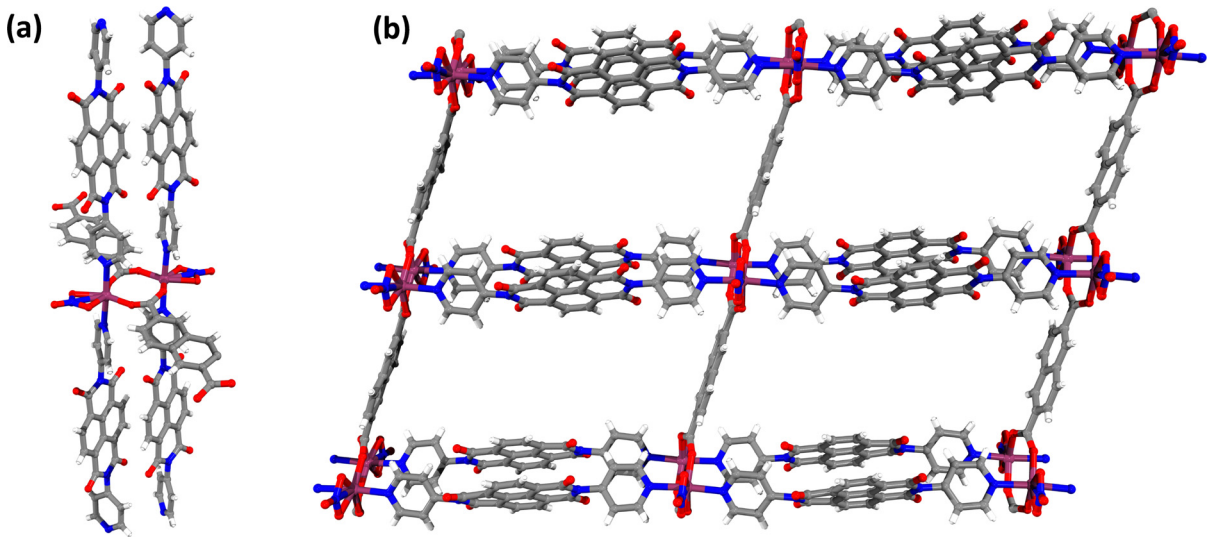

Fig. 1 (a) Coordination environment around the Co(II) metal in the 2D-Co MOF. (b) The MOF displays the connectivity of 2,6-NDC^{2-} and DPNDI ligands to form a 2-D layered structure. C, H, N, O and Co atoms are shown in grey, white, blue, red and plum colours, respectively. Solvent molecules have been removed for clarity.

$[Co(NO_3)_2{\cdot}6H_2O]$, acid linker (2,6-NDC) and N-based linker (DPNDI) in DMF and methanol at 80 °C. SC-XRD analysis revealed that the MOF crystallizes in the triclinic $P\bar{1}$ space group. The asymmetric unit consists of two cobalt atoms, two 2,6-NDC^{2-} ligands, four DPNDI ligands, and two nitrate groups attached to the metal cluster. Fig. 1a depicts that each Co(II) center is six coordinated by two nitrogen atoms from DPNDI ligands, one oxygen atom each from two 2,6-NDC^{2-} ligands and a nitrate group *via* two oxygen atoms. The Co–O and Co–N bond distances are in the range of 1.987(0)–2.194(6) Å and 2.133(2)–2.561(6) Å, respectively. Fig. 1b depicts the 2D layer structure.

After the careful crystallographic examination of the MOF system, the bulk purity of the as-synthesized MOF sample was checked with the help of PXRD analysis. The obtained PXRD patterns were compared with the simulated patterns and the analysis shows that the experimental PXRD patterns are consistent with the simulated patterns confirming the phase purity of the as-synthesized MOF sample (Fig. 2a). Furthermore, the thermal stability of the MOF sample was examined in the temperature range of 30 °C to 800 °C. The framework exhibited weight loss of 25% until 200 °C corresponding to the loss of solvent molecules and the framework collapsed beyond 350 °C. The framework has good stability up to 350 °C (Fig. S3, ESI†).

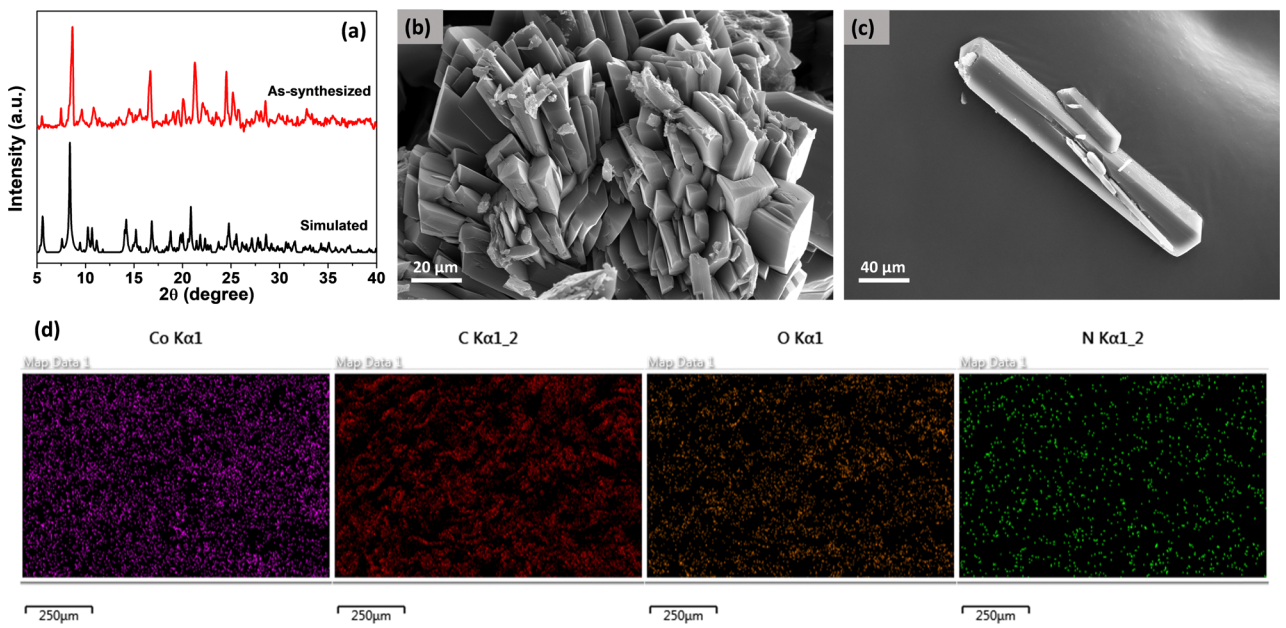

Fig. 2 (a) Simulated and as-synthesized PXRD patterns of 2D-Co MOF. (b) and (c) FE-SEM images of 2D-Co MOF. (d) Elemental mapping of 2D-Co MOF.

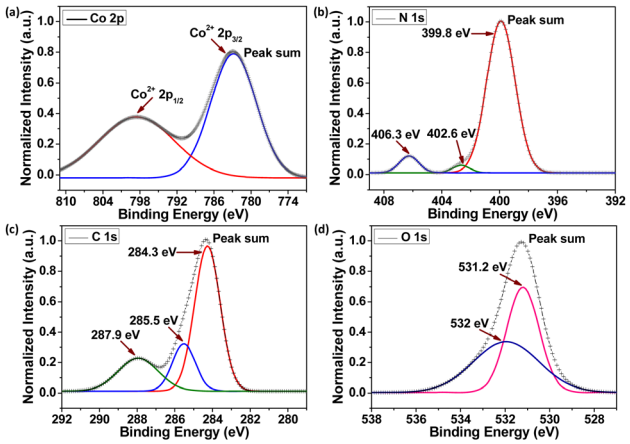

Fig. 3 XPS analysis of 2D-Co MOF depicting deconvoluted spectra of (a) Co 2p, (b) N 1s, (c) C 1s, and (d) O 1s.

The porosity of the framework was analysed with the help of N_2 adsorption measurements. The framework exhibited a surface area of 203.97 $m^2\ g^{-1}$ and a pore volume of 0.144 $cm^3\ g^{-1}$ (Fig. S4, ESI†). Fig. 2b, c and Fig. S5, ESI† obtained from FE-SEM clearly show that the MOF crystals are block-shaped with sizes ranging from 50 μm to 250 μm. Fig. 2d depicts the elemental mapping of the framework confirming the presence of Co, C, N and O elements.

The elemental composition is further supported by energy dispersive X-ray spectroscopy (EDAX) analysis as shown in Fig. S6 and Table S2, ESI.† Furthermore, XPS analysis of the framework confirmed the elemental composition and their chemical environment. Fig. S7, ESI† depicts the XPS survey spectrum displaying the characteristic binding energy peaks of the elements present in the framework. The deconvoluted XPS spectra of Co 2p, N 1s, C 1s and O 1s are represented in Fig. 3a–d. The deconvoluted Co 2p spectrum demonstrated the characteristic binding energy peaks of cobalt $2p_{1/2}$ and $2p_{3/2}$ at 798.5 eV and 782.85 eV, respectively, confirming the presence of cobalt as Co^{2+}. Binding energies of 284.3 eV, 285.5 eV and 287.9 eV, in the C 1s spectrum can be ascribed to C═C, C═N and N–$(C)_3$ or N–C═O bonds, respectively.[31] The O 1s spectrum is fitted with two peaks corresponding to the Co–O bond at 531.2 eV and C═O or O═C–O bond at 532 eV.[32] Similarly, the deconvoluted N 1s spectrum displays binding energy peaks at 399.8 eV, 402.6 eV and 406.3 eV, which can be assigned to the C═N–C bond, tertiary nitrogen N–$(C)_3$ groups and N–O bond of the nitrate group, respectively.[33]

3.2 Electrochemical studies

To investigate the electrochemical behaviour of the MOF, cyclic voltammetry (CV) of the bare GCE and MOF-coated GCE was recorded in PBS buffer (pH 7.02) in the potential window of −1 to +1.6 V with a sweep rate of 100 mV s^{-1}. The CV curve of the MOF exhibits an oxidation peak at a potential of +1.22 V due to the synergistic effect of redox-active linker DPNDI and cobalt metal (Fig. 4a). To determine the oxidation potential of NFZ, 300 μL of NFZ was added to the bare GCE, and an anodic peak at 1.1 V with a very small current response was observed.

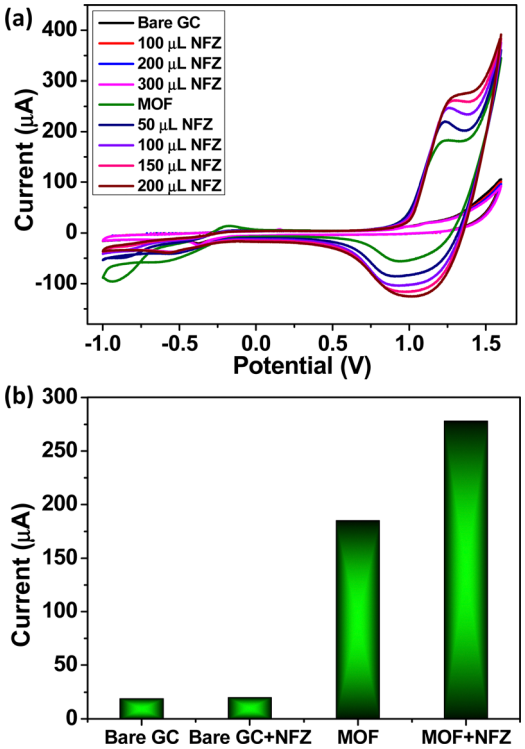

Fig. 4 (a) CV curve of the bare GCE and MOF/GCE on the addition of NFZ and (b) bar diagram representing the current response of the bare GCE and MOF/GCE towards NFZ.

Furthermore, the electrochemical sensing capability of the MOF/GCE towards NFZ was checked by adding incremental additions of NFZ. As depicted in Fig. 4a, on the addition of 50 μL of NFZ to the electrochemical cell, the MOF displays an anodic peak at +1.2 V, indicative of the oxidation of NFZ on MOF/GCE. This oxidation process leads to the generation of nitrogenous free radicals, followed by subsequent dimerization.[34] Fig. 4b shows that the current response of the MOF increased 1.5 fold from 185 μA to 278 μA on the addition of NFZ, whereas in the case of the bare GCE, hardly any change in the current response was observed. This clearly states that the MOF-modified GCE provides more active sites and promotes a facile pathway for faster electron transfer for the oxidation of NFZ on the electrode surface. Thus, the MOF acts as a potent electrocatalyst for the oxidation of NFZ.

3.3 Influence of pH and scan rate

The optimization of the pH of the electrolyte is important due to its significant effect on the electrocatalytic oxidation of the analyte. The current response of NFZ oxidation was checked with different pH electrolyte solutions (0.1 M PBS buffer) ranging from acidic to basic such as 5.0, 7.0, and 9.0. CVs were recorded in the above pH solutions in the presence of 50 μL NFZ at a scan rate of 100 mV s^{-1}. Fig. 5a shows that the current response started to increase from pH 5.0 to basic pH (pH 9.0), with the anodic peak potential of NFZ shifting to a more positive value. This shift illustrates the involvement of protons in the oxidation reaction.[34] Thus, considering the parameters

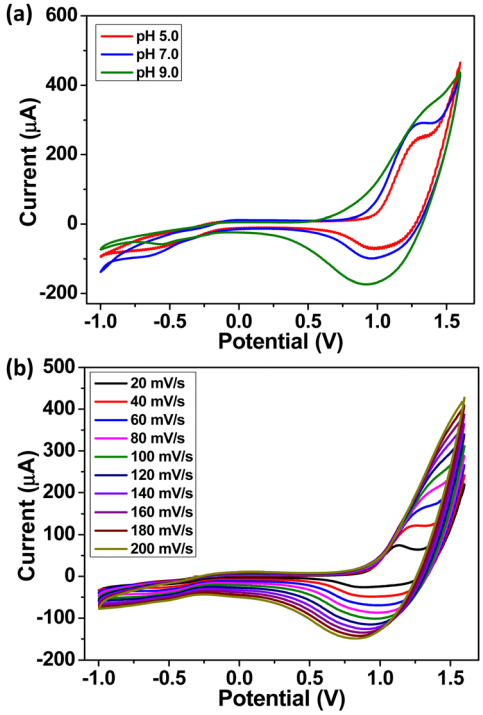

Fig. 5 (a) CV curve of MOF/GCE recorded at different pH values, and (b) CV curve of MOF/GCE at different sweep rates (20 to 200 mV s^{-1}) in the presence of 50 μL NFZ.

such as peak current, peak shape, and peak potential, pH 7.0 was chosen as the ideal pH condition of the buffer for effective electrocatalytic oxidation of NFZ. The influence of scan rate on the kinetics of an electrochemical reaction is studied with the help of the CV technique. The effect of scan rate on the oxidation of NFZ was investigated by recording the current response of the MOF in the presence of 50 μL of NFZ, as shown in Fig. 5b. Fig. 5b and Fig. S8, ESI† clearly depict that the oxidation peak current increased linearly on escalating the scan rates from 20 to 200 mV s^{-1} with excellent linear fitting of current vs scan rate with an R^2 value of 0.99. This demonstrates that the oxidation of NFZ on the MOF/GCE surface is an adsorption-controlled process.

3.4 Square wave voltammetry (SWV)

Detailed electrochemical sensing studies were carried out using more sensitive and dynamic techniques such as square wave voltammetry (SWV). The sensing ability of the MOF towards low concentrations of NFZ was checked in PBS buffer (pH 7.02) at a sweep rate of 100 mV s^{-1}. Fig. 6a shows that the current response of the MOF increased gradually with an increase in the concentration of NFZ. It is interesting to note that the MOF shows high sensitivity even to low concentrations (0.49 μM) of NFZ. Fig. 6b depicts that the oxidation peak current varied linearly with the NFZ concentration in the range of 0–2.5 μM with the R^2 value equal to 0.99. SWV studies of the MOF were also carried out with other concentration ranges of NFZ, as depicted in Fig. 6c and d. The current response of the MOF increased 3.5 fold with a very small addition of 4.9 μM NFZ and also the anodic peak current enhanced 5 fold from ~30 to ~160 upon the addition of 24.4 μM of NFZ solution. The above results demonstrate that the MOF acts as a highly efficient electrochemical sensor in detecting NFZ and also shows good sensitivity towards NFZ in the wide linear concentration range of 0–25 μM. The limit of detection (LOD) was calculated by using the slope value derived from the linear calibration plot mentioned above. This slope value was then substituted into the provided equation, LOD = 3s/m, where m

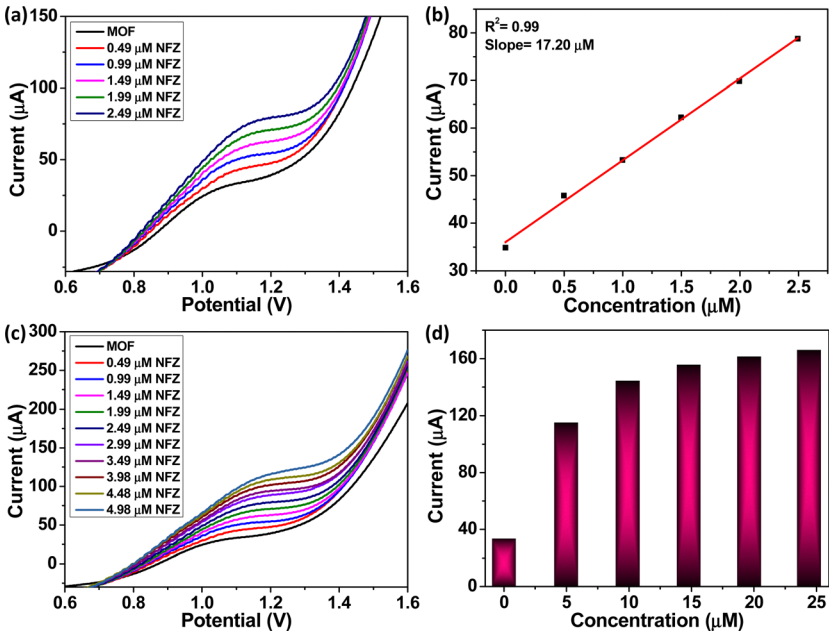

Fig. 6 (a) and (c) SWV curve of 2D-Co MOF towards incremental additions of NFZ, (b) linear plot for NFZ concentration *vs.* current response and (d) bar diagram for different concentrations of NFZ *vs.* anodic peak current.

Table 1 Comparison of electrochemical sensors for the detection of NFZ

Sensor	Material type	Electrochemical signal	Linear range (μM)	LOD (μM)	Ref.
Hollow MIL-101/GCE	MIL-101 modified electrode	Oxidation	0.03–55	0.01	34
$Pr_2Sn_2O_7$ NPs/GCE	Nanomaterial	Reduction	0.01–24	0.004	35
Carboxylic multi-walled carbon nanotubes/GCE	MWCNT	Reduction	5–1090	224	36
Boron-doped diamond electrode	Boron material	Reduction	0.99–11	340	37
AuNPs/UiO-66-NH_2/SPCE	Nanoparticles	Reduction	0.01–0.05	0.03	38
2D-Co MOF/GCE	MOF	Oxidation	0–25	0.04	This work

represents the slope and *s* denotes the standard deviation derived from five blank readings of the MOF. The limit of detection (LOD) was calculated to be 0.04 μM. The electrocatalytic performance of the MOF towards NFZ was compared with different materials such as composites, nanomaterials, carbon nanotubes, and boron-based materials (Table 1). It is noteworthy that there are hardly any MOF materials (pristine MOF without any composite preparation) reported as electrochemical sensors for the detection of NFZ and the MOF chosen for this study displayed excellent LOD and good electrocatalytic activity without any addition or modification with a secondary material.

3.5 Selectivity, repeatability and stability studies

Selectivity, repeatability, and stability are crucial parameters that are required for wider applicability and accurate analysis of real samples by a sensor. The repeatability and stability studies were carried out on the MOF/GCE using the SWV technique in the presence of 5 μM NFZ in PBS buffer (pH 7.02) at a sweep rate of 100 mV s^{-1}. Fig. 7a illustrates the repeatability studies conducted on the MOF for 10 consecutive runs. The relative standard deviation (RSD) of ~1% was observed, indicating a consistent oxidation peak current response from the MOF. The stability studies of the MOF/GCE sensor were carried out and the current response of the MOF was examined every day for 7 days. The sensor displayed an excellent current response of 97% even after 7 days with an RSD of ~1.2% (Fig. 7b).

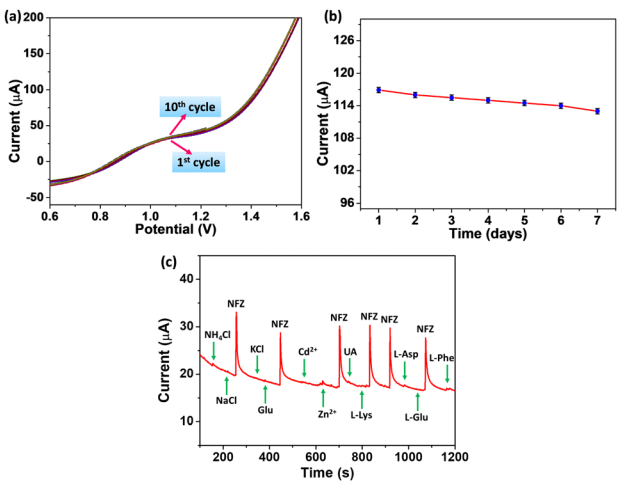

Fig. 7 (a) Repeatability studies of MOF/GCE in the presence of NFZ, (b) stability studies of MOF/GCE for 5 μM NFZ recorded for 7 days and (c) chronoamperometric studies of MOF/GCE recorded on the addition of NFZ and 100-fold excess concentration of possible interferents.

Furthermore, the selectivity of the MOF sensor was studied with the possible interferents that are found in real samples and can interfere with the detection of NFZ. The possible interferents chosen for the study include metal ions (Zn^{2+}, Cd^{2+}), metal salts (NaCl, NH_4Cl, KCl), biomolecules released in urine such as uric acid (UA), glucose (Glu) and common amino acids present in milk samples such as L-lysine (L-Lys), L-aspartic acid (L-Asp), L-glutamic acid (L-Glu) and L-phenylalanine (L-Phe). Selectivity experiments were recorded in PBS buffer (pH 7.02) with the help of the chronoamperometry technique. The amperometric response of the MOF was recorded in the presence of 2.5 μM NFZ at an applied potential of +1.2 V. The MOF sensor displayed a significant increase in the current intensity upon the introduction of a small concentration of NFZ. In contrast, the addition of a 100-fold excess concentration of interferents did not yield any discernible effect, as depicted in Fig. 7c. The above results confirm the remarkable selectivity of the MOF sensor in detecting NFZ and the feasibility of the MOF sensor for real-time studies.

3.6 Detection of NFZ in biological and food samples

To assess the practical feasibility of the MOF sensor in detecting NFZ, real-time experiments were carried out. Biological (human urine) and food (milk) samples were chosen for the study. The human urine and milk samples were diluted 100 times and the pH was adjusted to 7.02 before proceeding for analysis. The analysis was carried out using SWV and the current responses were recorded on the addition of as-prepared

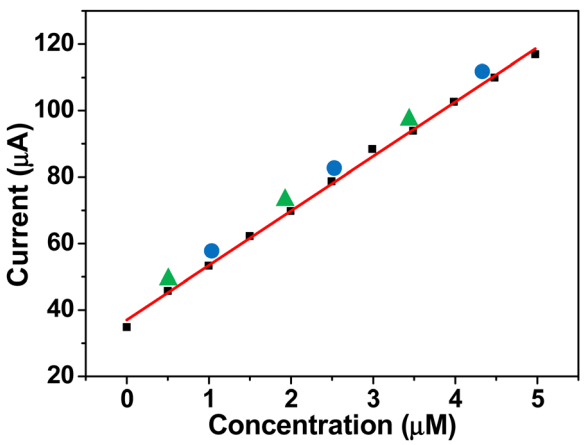

Fig. 8 Representation of the current response for spiked NFZ amounts in urine (▲) and milk (●) samples for calculating recovery concentrations using a calibration plot of NFZ.

Table 2 Electroanalytical detection of NFZ in real samples

Sample	Spiked (μM)	Found (μM)	Recovery (%)
Urine	0.49	0.51	96.08
	1.99	2.02	98.51
	3.49	3.53	98.86
Milk	0.99	1.04	95.19
	2.49	2.53	98.42
	4.48	4.52	99.11

real samples. However, the real samples did not exhibit any significant current change that might be attributed to the absence of NFZ. Hence, both the samples were spiked with known concentrations of NFZ, and the corresponding current responses were recorded. The obtained current responses from spiked samples were plotted and correlated with the calibration plot of current *vs*. NFZ concentration, as depicted in Fig. 8. The spiked amounts of NFZ and the recovered amounts were calculated using the standard addition method and the results are tabulated in Table 2. The observed recovery percentage of spiked amounts of NFZ in the real samples falls in the range of 96–99% with a minimal relative error of 0.2% making the sensor efficient in quantitative determination of NFZ. These results indicate that the sensor demonstrates high efficacy in accurately quantifying NFZ in biological and food samples.

4. Conclusions

To summarize, a novel 2D-Co MOF was synthesized using a mixed-linker approach. A comprehensive structural investigation of the framework was carried out using XRD, TGA, BET, FE-SEM, and XPS. Furthermore, the electrochemical properties of the MOF were studied using CV and SWV techniques. A MOF-based electrochemical sensor was developed and explored for the detection of NFZ. The MOF sensor displayed high sensitivity towards NFZ with very low detection limits of 0.04 μM. The sensor exhibited good repeatability and stability towards NFZ for a period of 7 days. The sensor also presents high selectivity towards NFZ even in the presence of potential interferents that could practically hamper the analysis of NFZ in real samples. Additionally, the MOF sensor demonstrated great potential towards the detection of NFZ residues in human urine and milk samples. We strongly believe that these results may open up new avenues for the advancement of MOF sensors in the field of food safety and offer solutions to combat antibiotic pollution and safeguard public health.

Author contributions

TL conceptualized the idea, carried out all the experimental work and wrote the manuscript. HA discussed the results and corrected the manuscript for further improvement. All authors have given approval to the final version of the manuscript.

Data availability

The data supporting this article have been included as part of the ESI.† Crystallographic data for 2D-Co MOF has been deposited at the CCDC under deposition number 2391733.†

Conflicts of interest

There are no conflicts to declare.

Acknowledgements

H. A. thanks DST-SERB for funding (grant sanction order number (CRG/2022/004414)) and T. L. thanks BITS-Pilani, Hyderabad for the research fellowship. The authors thank BITS-Pilani, Hyderabad Campus Central Analytical Laboratory for access to all the state-of-the-art facilities.

References

1 T. M. Rawson, L. S. P. Moore, N. Zhu, N. Ranganathan, K. Skolimowska, M. Gilchrist, G. Satta, G. Cooke and A. Holmes, *Clin. Infect. Dis.*, 2020, **71**, 2459–2468.
2 R. K. Langbehn, C. Michels and H. M. Soares, *Environ. Pollut.*, 2021, **275**, 116603.
3 J. L. Martinez, *Environ. Pollut.*, 2009, **157**(11), 2893–2902.
4 S. I. Polianciuc, A. E. Gurzău, B. Kiss, M. G. S. Tefan and F. Loghin, Antibiotics in the environment: causes and consequences, *Med. Pharm. Rep.*, 2020, **93**, 231.
5 R. S. Vardanyan and V. J. Hruby, *Synthesis of Essential Drugs*, Elsevier, Amsterdam, 2006, pp. 499–523.
6 A. Kaufmann, P. Butcher, K. Maden, S. Walker and M. Widmer, *Anal. Chim. Acta*, 2015, **862**, 41–52.
7 A. Joshi and K. H. Kim, *Biosens. Bioelectron.*, 2020, **153**, 112046.
8 C. Liu, B. Li, M. Liu and S. Mao, *Sens. Actuators, B*, 2022, **369**, 132383.
9 B. Wang, X. L. Lv, D. W. Feng, L. H. Xie, J. Zhang, M. Li, Y. B. Xie, J. R. Li and H. C. Zhou, *J. Am. Chem. Soc.*, 2016, **138**, 6204–6216.
10 C. Wang, Q. L. Li, B. L. Wang, D. D. Li and J. H. Yu, *Inorg. Chem. Front.*, 2018, **5**, 2183–2188.
11 W. W. Bian, Z. Liu, G. Lian, L. Wang, Q. L. Wang and J. H. Zhan, *Anal. Chim. Acta*, 2017, **994**, 56–64.
12 L. Q. Sheng, M. M. Chen, S. S. Chen, N. N. Du, Z. D. Liu, C. F. Song and R. Qiao, *Food Addit. Contam.: Part A*, 2013, **30**, 2114–2122.
13 C. W. Tsai, C. H. Tang and W. H. Wang, *J. Food Drug Anal.*, 2010, **18**, 98–106.
14 W. P. Lustig, S. Mukherjee, N. D. Rudd, A. V. Desai, J. Li and S. K. Ghosh, *Chem. Soc. Rev.*, 2017, **46**, 3242–3285.
15 M. Lu, Y. Deng, Yi Luo, J. Lv, T. Li, J. Xu, S. W. Chen and J. Wang, *Anal. Chem.*, 2019, **91**, 888–895.
16 B. S. He and X. Z. Dong, *Anal. Methods*, 2018, **10**, 1372–1378.
17 Ü. Anik, S. Timur and Z. Dursun, *Microchim. Acta*, 2019, **186**, 196.

18 S. H. Chiu, Y. L. Su, A. V. T. Le and S. H. Cheng, *Anal. Bioanal. Chem.*, 2018, **410**, 6573–6583.
19 F. Ye, J. Z. Huang, Y. Q. Xu, Q. Zeng, J. M. Nan and L. S. Wang, *Anal. Lett.*, 2018, **51**, 728–741.
20 C. L. Brito, E. I. Ferreira and M. A. La-Scalea, *J. Solid State Electrochem.*, 2020, **24**, 1969–1980.
21 B. S. He and X. Z. Dong, *Anal. Methods*, 2018, **10**, 1372–1378.
22 A. Rahi, N. Sattarahmady, R. Dehdari Vais and H. Heli, *Sens. Actuators, B*, 2015, **210**, 96–102.
23 L. D. Ji, J. Wang, K. B. Wu and N. J. Yang, *Adv. Funct. Mater.*, 2018, **28**, 1706961.
24 T. Leelasree, M. Dixit and H. Aggarwal, *Chem. Mater.*, 2023, **35**, 416–423.
25 Y. Li, Y. T. Wang, W. D. Fan and D. F. Sun, *Dalton Trans.*, 2022, **51**, 4608–4618.
26 T. Leelasree, P. N. Sidhartha, M. Tathacharya, K. N. Chappanda and H. Aggarwal, *J. Mater. Chem. C*, 2024, **12**, 7295–7305.
27 H. Li, K. Wang, Y. Sun, C. T. Lollar, J. Li and H. C. Zhou, *Mater. Today*, 2018, **21**, 108–121.
28 G. Radha, K. Sathish Kumar, Karumbaiah N. Chappanda and H. Aggarwal, *J. Phys. Chem. C*, 2023, **127**, 8864–8872.
29 T. Leelasree, S. Goel and H. Aggarwal, *ACS Appl. Nano Mater.*, 2022, **5**, 16753–16759.
30 S. Guha, F. S. Goodson, L. J. Corson and S. Saha, *J. Am. Chem. Soc.*, 2012, **134**, 13679.
31 X. Yan, T. Xu, G. Chen, S. Yang, H. Liu and Q. Xue, *J. Phys. D: Appl. Phys.*, 2004, **37**, 907.
32 Y. Wang, J. Yu, W. Peng, J. Tian and Y. Chun, *Sci. Rep.*, 2019, **9**, 5932.
33 S. Ravi, S. Zhang, Y. R. Lee, K. K. Kang, J. M. Kim, J. W. Ahn and W. S. Ahn, *J. Ind. Eng. Chem.*, 2018, **67**, 210–218.
34 T. Gan, J. Li, L. Xu, Y. Yao and Y. Liu, *J. Electroanal. Chem.*, 2019, **848**, 113287.
35 R. Rajakumaran, R. Sukanya, S. M. Chen, R. Karthik, C. B. Breslin and P. M. Shafi, *Inorg. Chem.*, 2021, **60**, 2464–2476.
36 B. S. He and M. Li, *Int. J. Electrochem. Sci.*, 2018, **13**, 4171–4181.
37 M. S. D. Juliao, E. I. Ferreira, N. G. Ferreira and S. H. P. Serrano, *Electrochim. Acta*, 2006, **51**, 5080–5086.
38 R. Rani, A. Deep, B. Mizaikoff and S. Singh, *J. Electroanal. Chem.*, 2022, **909**, 116124.